Crashworthiness of poplar wood veneer tubes

R. Guélou, Florent Eyma, Arthur Cantarel, Samuel Rivallant, Bruno Castanié

Crashworthiness of poplar wood veneer tubes

R. Guélou[a], F. Eyma[a], A. Cantarel[a], S. Rivallant[a], B. Castanié[a,*]

[a]Institut Clément Ader (ICA), ISAE, CNRS UMR 5312-INSA-Mines Albi-UPS, Toulouse, France

* Corresponding author: bruno.castanie@insa-toulouse.fr

Keywords: Wood, Poplar, Crushing, Energy absorption, Static, Dynamic

Abstract

This work studies the potential of using wooden tubes for crash applications. The tubes were made from 1 mm thick “I214” poplar veneers, according to different stacking sequences. Four configurations were characterized under static crushing (5 mm/min) and the one that performed best ($[90/0_4/90]$) was chosen to undergo dynamic tests under a drop weight tower (5.7 m/s). This configuration presents significant energy absorption performance in static (31.6 J / g) and in dynamic (28.5 J / g) crushing for a material that is natural, ecological (low carbon footprint), recyclable, and low cost in comparison with other materials such as composite materials. As with composites, the position, number, and orientation of the plies directly affect the amount of energy absorbed. The use of poplar, one of the weakest woods in mechanical terms, shows the possibilities of wood for this use.

1. Introduction

Wood, by its nature, is an ecological material that has a very low grey energy (energy required from the creation of the raw material to the installation of the finished product) due, in particular, to its capacity to store carbon [1, 2]. It is also a recyclable material that, once it reaches the end of its life, can be used for the manufacture of particle boards or for energy recovery (heating). Additionally, it is, a material that is much cheaper than others. Wood or plywood are generally used in construction and furniture but also have applications in other fields, such as civil light aviation, boating, and the nuclear industry or, in the past, the automobile industry [3- 6]. Plywood has good weight specific mechanical properties under bending, tension, compression and shear [7].

There are few studies on the impact or crash behaviour of wood. Johnson analysed the problem in 1986, mainly from a historical point of view in the naval field [8]. Some studies have been carried out to study the dynamic behaviour of wood via tests on Hopkinson bars [9-12] but few dynamic studies have been carried out on drop weight apparatus. Adalian and Morlier [13], however, studied the behaviour, in the longitudinal and tangential directions, of poplar in the form of massive rectangular specimens with this kind of tests. The objective of their study was to obtain enough static and dynamic compression data to be able to model wood as a shock absorber. The force-displacement curve showed that the dynamic performance of poplar was slightly better than its static performance in the longitudinal or tangential direction (Plateau force, Energy Absorbed (EA) or Specific Energy Absorbed (SEA)). There is now renewed interest in these materials and the issue [15-18]. Some very interesting studies have also been conducted on the dynamic behaviour of coconut woods [19-21].

Susainathan et al. studied various configurations of sandwich plates with composite skins (aluminium, carbon, glass, and flax) and a plywood core subjected to low speed / low energy impacts [16]. They demonstrated that, as a core material, it was better to have a plywood that multiplies the interfaces (i.e. the number of plies) to improve the transverse behaviour and thus the impact response. These authors also investigated the numerical modelling of this type of impact in a preliminary manner, but this is a new field requiring a very great amount of characterization work [17]. It can therefore be argued that experimental studies on these types of materials should be done first. Then the same authors tested sandwiches and plywood alone in compression and compression after impact [18]. The two plywoods, alone or sandwiched with aluminium, flax or glass skins, showed a remarkable response in compression after impact of the panels with, in particular, the presence of a plateau on the force-displacement curve and a high residual resistance. Because of these good characteristics of plywood after impact and compression, the question arises as to the use of these structures for crash applications.

Given the small number of studies for wood, it is wise to focus on composite materials, which will serve as a reference for this study because their use has increased significantly in recent years despite their complexity [22]. In the crash domain, the low density and high specific resistances of composite materials make it possible to obtain very interesting energy absorption when they are appropriate to the failure mode [23-34]. The energy absorption potential of a material is assessed using the SEA (Specific Energy Absorption, which corresponds to the energy absorbed per unit of mass). The different configurations and numerous parameters that vary among the studies available in the literature generate a wide range of SEA for composite materials. Guillon [23] showed that, for carbon-epoxy plates, the SEA varied according to the main mode of damage. A pure splaying mode generated a low SEA, between 4 and 7 J/g. The SEA was from 33 to 50 J/g for a failure mode with predominant fragmentation, and from 10 to 15 J/g in the case of a combination of these two modes (known as brittle fracture mode). For circular carbon-epoxy tubes with an internal diameter of 50 mm oriented at ± 15°, Wang et al. [26] obtained a SEA of 94 J/g, and a SEA of 73 J/g for an orientation of ± 45°. Hamada et al. [27], also on circular carbon tubes with an internal diameter of 50 mm [± 45°], found a SEA of 53 J/g. When the carbon fibres were combined with a PEEK resin, a significant improvement was observed, with a SEA of 180 J /g. Glass fibres have interesting SEA, and Hu et al. [28] obtained 77 J/g on 50 mm diameter circular tubes oriented at ± 15°. With glass fibre tubes 55 mm in internal diameter, Song [29] reached 50 to 60 J/g depending on the trigger, with fibres oriented at [±45°] and in local buckling mode. Yan and Chouw [30] obtained an optimal configuration reaching 42 J/g on circular tubes with an internal diameter of 36 mm, made of flax fibres with [0/90] stacking. For tubes, the failure mode corresponding to the formation of symmetrical or asymmetrical folds creating multi-lobes (accordion mode) is generated by local buckling and concerns ductile materials such as aluminium or Kevlar fibres (Fig. 1 (a) and (b)). The additional folds leading to the formation of the accordion mode are created by a succession of local buckling events. During this failure mode, energy is absorbed by the plasticization of the folds. Farley and Jones called this mode "folding mode" or "local buckling mode" [31].

The “splaying crushing mode” (name given by Hull [32]) or “lamina bending mode” (name given by Farley and Jones [31]) concerns fragile materials. Splaying corresponds to a division of the walls into two parts (Fig 1 (c)). The splaying mode starts with an interlaminar crack or a delamination, which propagates and separates the structure into two parts. The bending of these two branches causes fibres to break, allowing the initial crack to propagate. In this failure mode, energy is absorbed by friction (delaminated plies, debris trapped inside), by matrix cracking, and by fibre failure. The division of the structure into two branches causes the tube to split, generating the appearance of petals. The fragmentation mode also concerns fragile materials and appears after numerous cracks of the order of magnitude of the thickness of the plies (Fig. 1 (d)). The cracks divide the crushing front into multiple pieces of falling debris, which ruins the structure. Most of the time, for fragile composites, crash failure does not occur in a pure splaying or fragmentation mode but as a mixture of the two. The combination of these two modes (splaying and fragmentation) is called “brittle fracturing mode” by Farley and Jones [31].

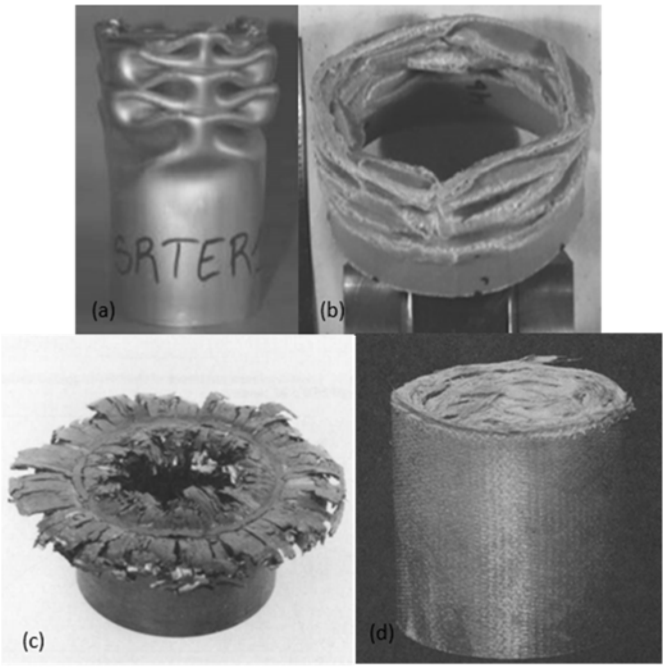

Fig. 1 : « Diamond » failure mode (a) AL6060 tube reproduced from [39]) (b) Kevlar/epoxy tube (reproduced from [40]) Splaying mode (c) CFRP tube (reproduced from [27]) Fragmentation mode (d) GFRP tube (reproduced from [32])

Kindervater [33] shows that the specific energy absorbed is dependent on the geometrical shape of the crash-box. Compared to a circular tube, a square tube shows 20% less SEA, and a rectangular tube 50% less. Hull [32] also demonstrated the importance of ply orientation on unidirectional glass or carbon fibre laminate tubes. The SEA varies very strongly depending on the orientation, the position, and the number of plies. The static SEA can vary from 6 to 88 J/g. He also defines a "hoop effect", which describes an improvement in the absorption of energy due to stabilization of the crushing when the fibres oriented at 0° are confined between layers oriented at 90°. Similarly, Thornton and Edwards [34], using unidirectional glass fibre tubes, have shown the importance of both the "hoop effect" and the presence of fibres oriented at 0°. If the position of the plies is changed to 0° or 90°, the SEA varies by 50%.

The two objectives of the present study are therefore:

- To evaluate the energy absorption capacity under crash of wood in the form of tubes made from poplar veneers, in static and dynamic crushing, and thus to compare not only the performance levels but also the failure modes. Poplar was chosen from among the many wood species available because of its low cost, its ease of manufacture and its availability in the form of plies. As its mechanical characteristics are among the weakest, the results obtained can be considered to represent the least advantageous possibilities of wood.
- To understand the mechanisms of damage and energy absorption of these tubes and compare them with the findings of other crash studies on known materials, such as composite or metallic materials.

2. Materials and Methods

2.1. Materials and manufacturing.

The tubes were manufactured from I214 poplar veneers supplied by the Garnica company [35]. The thickness of the plies was 1 mm. All the tubes produced had 6 plies, with an internal diameter of 50 mm for a length of 120 mm. The total thickness of the tubes was between 6.25 and 6.90 mm. Depending on the configuration and the constraints of the veneer bending process, the thicknesses varied slightly. The average relative density of the tubes (veneers and glue) was 544 kg/m^3. The glue used to bond the veneers was Kleiberit PUR 510 Fiberbond, a one-component glue based on polyurethane hardening by reaction with humidity, having an areal density of 250 g/m^2. The static and dynamic charcaterization of the individual ply was not performed in this study and is out-of-the scope of the objective of this paper. Unlike classical composite materials, the need for characterization in the industry is poor at this level and until the research is also not so developped. Nevertheless, only static bending tests are available in the literature [36, 37] and are summarized in the in Table 1:

		Bending		
		Modulus (MPa)	Strength (MPa)	Ref
One-ply (4.3 mm)	Hybrid poplar clone 15 303	5 862	50	(Fang et al. 2012)
Plywood (12 mm)	Poplar clone "I-214'	4 153	24.8	(Baldassino, Zanon, et Zanuttini 1998)

Table. 1: Some results on poplar material properties [36, 37].

Regarding the forming of the tubes, the stacking of layers at 0° was performed dry. For layers at 90°, it was necessary to immerse the veneers in water before forming them directly on a mould. They were then dried at 50 °C for 3.5 hours. Once dry, the veneers were bonded and rolled up using heat-shrinkable bands, which provided pressure during the crosslinking of the glue at 120 °C for 20 min. The relative humidity of "dry" veneers oriented at 90 ° was between 5.5 and 12.7%, and was between 8.8 and 9.8% for veneers oriented at 0°. The tubes were finally cut to the desired length. At one end (Fig.2), a 45° chamfer was milled over the entire thickness of the tube in order to initiate failure and reduce the load peak [38].

Four configurations were used to study the effect of the stacking sequence: $[0_6]$, $[90/0_4/90]$, $[90_2/0_2/90_2]$, and $[0_4/90_2]$, 0° corresponding to the longitudinal axis of the tube. For each configuration, three tubes were crushed in order to assess the repeatability of the results.

Fig. 2: Pristine sample [0_4/90_2] - #2

2.2. Static tests

The tests were carried out at a speed of 5 mm/min on an MTS system tension machine equipped with a 100 kN load cell and a displacement sensor. The tubes were crushed over ¾ of their length, i.e. 90 mm, which was long enough for a stable crushing mechanism to be observed when it existed.

Generally, during a stable crash, three phases are observed on the force-displacement curve: a pseudo-linear part up to a peak force, which is followed by the first damage and a transition phase and, finally, a plateau phase. In our case, the apparent linearity of the force-displacement curve corresponded rather to a pseudo-linear phase because, in reality, the chamfer of the tube started to be damaged. Several quantities and performance criteria can be extracted from the force-displacement curve obtained during the crash. The peak force is noted F_{max}. When a force plateau exists, the average force in the plateau is called $F_{plateau}$. The CFE (Crush Force Efficiency) can then be defined as the ratio between the average force and the maximum force ($F_{plateau}$ / F_{max}). In general, when designing a shock absorber [39], a CFE as close to 1 as possible is sought, to limit the forces in the rest of the structure during a crash.

With regard to energies, two quantities were defined. The first was the total energy dissipated in the tube. It allowed direct comparison of the absorption capacities of various tubes. As the crushed length varied somewhat according to the tests (between 80 and 90 mm), the total energy was calculated only on the first 80 mm crushed. It is written E_{tot_80mm} here (see Fig. 3 (b)).

In this paper, the specific absorption energy was calculated, not from the entire curve, but only from the stabilized phase of the crushing (Fig. 3 (a)), which therefore corresponded to established absorption mode and damage mechanisms. Thus, we also defined the energy absorbed in the plateau ($EA_{plateau}$), which depends on the real length of the stable phase ($L_{plateau}$), and deduced the specific absorption energy during the plateau: $SEA_{plateau} = \frac{F_{plateau}}{\rho \times S}$, in J/g, with ρ the average density of the tube (glue + veneers) and S its cross section.

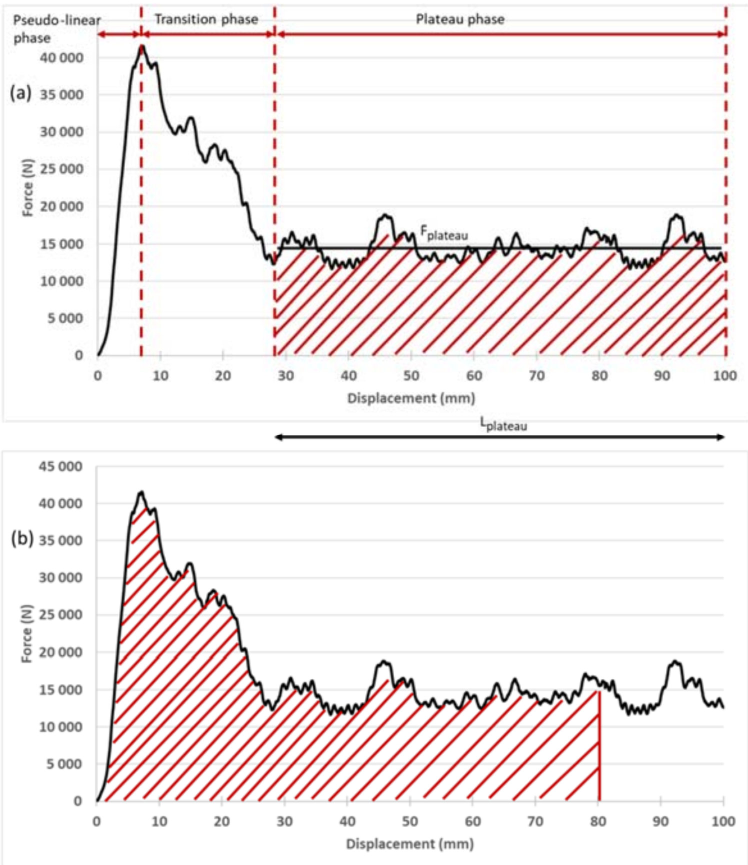

Fig. 3: Calculation methods for the Energy Absorbed. (a) $EA_{plateau}$ only, (b) EA_{tot_80mm}

2.3. Dynamic tests

The dynamic tests were carried out using a drop weight tower, at 5.7 m / s (Fig. 4). These tests were interrupted for post-mortem observations on the samples. They were also filmed using a high-speed camera during the entire crash.

The operating principle of the assembly was as follows: the mass used (180 kg) was calculated so that the kinetic energy available during the impact was significantly greater than the energy necessary to crush 85 mm of the tube. We thus obtained a test with an almost constant crushing speed. To stop the crushing after approximately 85 mm, a stop system was used, which allowed the excess energy to be transferred into an absorber (Nomex honeycomb block) located under the sample (Fig. 4).

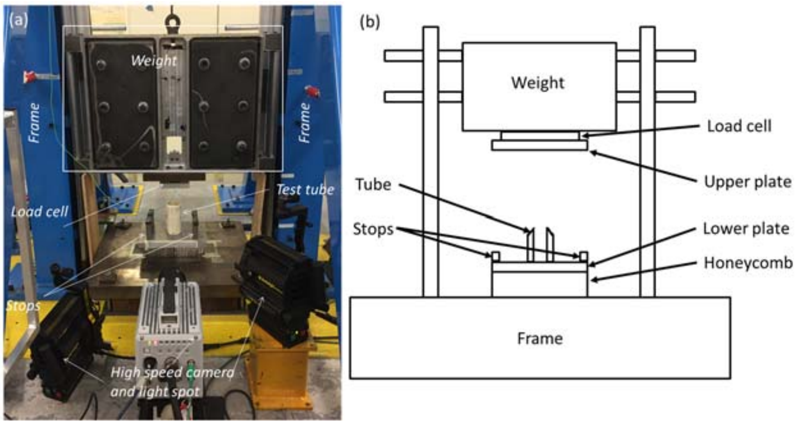

Fig. 4: (a) Overview photograph of the dynamic testing setup, (b) Schematic representation

A force sensor located between the mass and the upper crushing plate made it possible to obtain the crushing force with an acquisition frequency of 1 MHz. The displacement was calculated by double integration of the force from knowledge of the initial speed given by an optical sensor. No filtering was performed for data extraction. The high speed camera and the force signal were synchronized in order to be able to link the images of the crushing front with the force-displacement curve. A redundant calculation of displacement was also carried out using the camera images for a few samples to verify the accuracy of the double integration method.

3. Results and discussion

All data are available in Table. 2 and Force-displacement curves for the static response are shown in Fig 5.

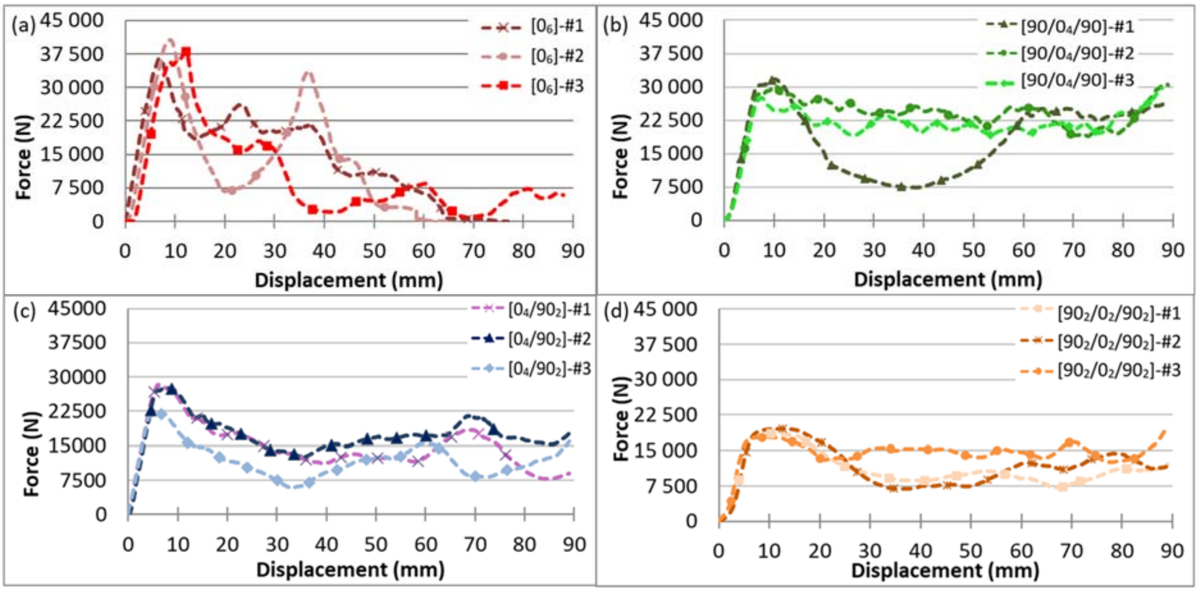

Fig. 5: Static force-displacement curves for tubes (a) $[0_6]$ (b) $[90/0_4/90]$ (c) $[0_4/90_2]$ (d) $[90_2/0_2/90_2]$

		g	mm	N	mm	N	/	J	J	J/g
		Mass	Thickness	F_{max}	$L_{plateau}$	$F_{plateau}$	CFE	$EA_{plateau}$	EA_{tot_80mm}	$SEA_{plateau}$
Static tests	$[0_6]$ - #1	77.4	6.7	36 403	/	/	/	/	/	/
	$[0_6]$ - #2	76.0	6.8	40 667	/	/	/	/	/	/
	$[0_6]$ - #3	75.3	6.6	38 067	/	/	/	/	/	/
	Average	76.2	6.7	38 379	/	/	/	/	/	/
	Standard deviation	1.07	0.09	2 149	/	/	/	/	/	/
	$[90/0_4/90]$ - #1	76.9	6.9	31 722	74.9	17 039	0.54	1 276	1 368	25.4
	$[90/0_4/90]$ - #2	77.8	6.9	30 220	77.6	24 092	0.80	1 869	1 858	35.5
	$[90/0_4/90]$ - #3	74.9	6.7	27 569	78.1	21 926	0.80	1 712	1 670	33.8
	Average	76.6	6.8	29 837	76.9	21 019	0.71	1 619	1 632	31.6
	Standard deviation	1.8	0.10	2 103	1.7	3 613	0.15	307	247	5.4
	$[90_2/0_2/90_2]$ - #1	70.6	6.7	17 798	68.9	14 592	0.82	1 005	1 154	22.2
	$[90_2/0_2/90_2]$ - #2	73.1	6.6	19 541	64.2	10 312	0.53	662	923	16.3
	$[90_2/0_2/90_2]$ - #3	75.7	6.8	18 514	53.7	9 542	0.52	512	866	15.6
	Average	73.1	6.7	19 403	62.2	11 482	0.62	726	981	18.0
	Standard deviation	2.55	0.11	876	7.18	2 721	0.17	253	152	3.6
	$[0_4/90_2]$ - #1	73.5	6.5	28 311	55.3	12 680	0.45	701	1 241	19.9
	$[0_4/90_2]$ - #2	73.3	6.5	27 581	53.9	16 779	0.61	905	1 400	26.4
	$[0_4/90_2]$ - #3	72.4	6.6	22 039	56.7	10 991	0.50	624	939	17.5
	Average	73.0	6.6	25 977	55.3	13 483	0.52	743	1 193	21.3
	Standard deviation	0.59	0.01	3 430	1.4	2 976	0.08	145	234	4.6
Dynamic tests	$[90/0_4/90]$ - #1	72.0	6.5	41 601	51.5	14 454	0.35	744	1 462	23.2
	$[90/0_4/90]$ - #2	72.5	6.3	45 213	54.9	14 515	0.32	797	1 428	23.1
	$[90/0_4/90]$ - #3	71.0	6.3	44 762	54.0	18 997	0.42	1 025	1 705	31.0
	$[90/0_4/90]$ - #4	72.7	6.3	44 947	55.9	21 143	0.47	1 183	1 759	33.7
	$[90/0_4/90]$ - #5	75.4	6.4	46 717	55.8	22 716	0.49	1 267	1 842	34.9
	$[90/0_4/90]$ - #6	73.2	6.7	47 267	55.2	15 811	0.34	873	1 512	24.9
	Average	73.7	6.5	45 084	54.6	17 939	0.40	982	1 618	28.5
	Standard deviation	1.44	0.16	1 951	0.4	3 538	0.07	212	173	5.4

Table. 2: Static and Dynamic test results.

3.1. Static crushing

3.1.1. Results for $[0_6]$ Tubes.

The first damage corresponded to the appearance of longitudinal cracking along the fibres after the peak load (Fig. 5 (a)). These cracks cut the tube into several sections (Fig. 6). Then each section began to bend until it broke. The longitudinal crack spread over a large part of the tube, leading to a total loss of stiffness of the tube and marking a crushing force close to 0. For these types of tubes, the absence of a plateau is to be noted and, therefore, energy absorption performance is difficult to exploit and the expression does not necessarily have a clear meaning (Fig. 5 (a)). Delamination between layers also occurred, and fragmentation could also be observed following these failures in fibres at 0° stressed under bending (Fig. 6). It generated the formation of bundles, five large ones (almost half the length of the tube) being counted for tubes # 1 and # 3, and 6 for tube # 2. This failure mode was observed on the three tubes and was repeated although certain cracks did not start to form at the same time, which explains the shift in the force-displacement curves (Fig. 5 (a)). However, this is a very unstable mode of failure and results in oscillations generating a small amount of absorbed energy due to the force falling to 0 N. For this configuration, the energy absorption is not optimal.

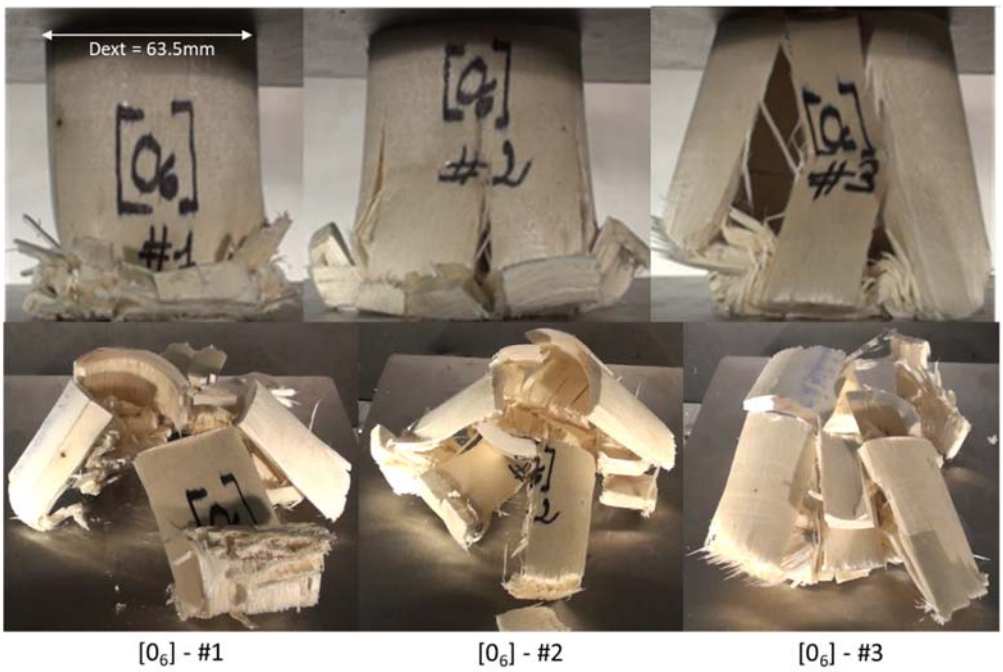

Fig. 6: Failure patterns of $[0_6]$ tubes under a crush displacement of 40 mm and post-mortem patterns.

3.1.2. Results for [90/0_4/90] Tubes.

The advantage of this configuration was that it permitted observation of the influence of the orientation of the outer and inner layers at 90°, which creates a confinement of the inner layers at 0°. For the first tube (# 1) failure initiation occurred in its middle (Fig. 7 (a)). For the other two other tubes (# 2 and # 3), folds occurred in an asymmetric manner. Once the first fold was created, the tube returned to its initial configuration and could sustain crushing on a portion of the tube that had not yet been damaged. The first fold appeared as soon as the chamfer was crushed. During the crushing and because of the creation of the folds, the fibres at 90° broke and the fibres at 0° bent until they ruptured. The failure modes of the three tubes was quite similar: even though the damage of tube # 1 began halfway up the tube, the same mode of failure occurred during the crushing, which explains the same level of force obtained at the end of the compression. However, the number of folds was not identical in the three tubes.

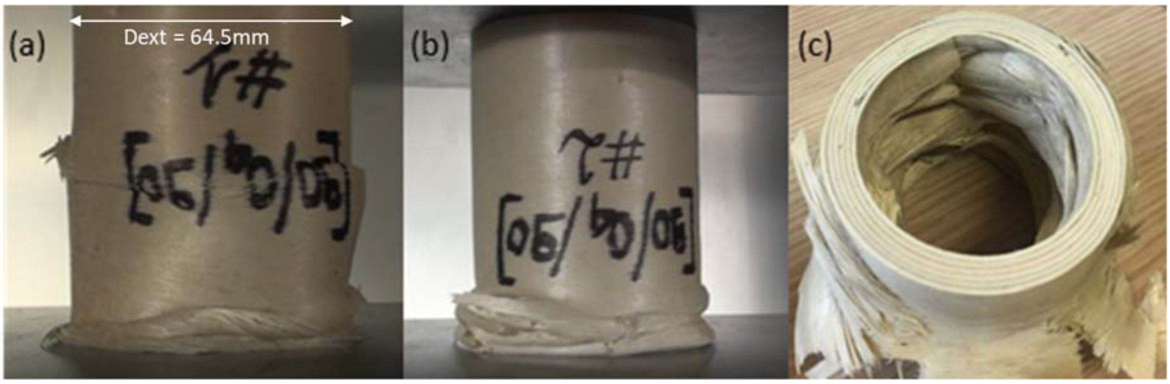

Fig. 7: (a) Failure mode of tube [90/0_4/90] - #1 after 20 mm of crushing; (b) tube [90/0_4/90] - #2 after 32 mm of crushing and fold creation; (c) tube [90/0_4/90] - #3 post-mortem pattern

The resulting failure mode can be compared to the diamond failure mode [40-42] in tubes made of metallic material, for example aluminium (Fig. 1 (a)), or Kevlar-epoxy composites (Fig. 1 (b)).

The force-displacement curve (Fig. 5 (b)) exhibits a load peak followed by the first damage. In configuration [90/0_4/90], unlike configuration [0_6], a plateau occurs after the load peak, except for tube #1. For this tube, as already mentioned, the initiation of failure occurred in the middle. So, the first fold did not form from the start of the crushing and was observed later, with a drop in force at the level of the plateau between about 20 and 50 mm. Then, an increase in the force was observed up to the plateau level for tubes # 2 and # 3. For wood, introducing fibres at 90° helped to stabilize the crushing by confining the fibres at 0°. The stabilization of the crushing linked to the layers at 90° thus prevented transverse longitudinal cracks, made it possible to obtain a plateau on the force-displacement curve (non-existent for the tubes [0_6]) and significantly increased the energy absorbed (1 619 J) and the SEA (31.6 J / g). These tests also showed a relatively low initial peak force compared to the plateau value, resulting in a relatively high CFE (0.71)

3.1.3. Results for [$90_2/0_2/90_2$] Tubes.

This configuration showed the influence of the number of layers at 90° on energy absorption. The initiation of damage on tubes # 1 and # 3 was unstable. In fact, it was probably due to an interaction between local buckling at the centre of tubes and overall buckling (Fig. 8). The ruin of tube # 1 spread with interpenetration while the ruin of tube # 3 spread on the opposite side of the chamfer. The damage initiation in tube # 2 occurred as expected on the chamfered side. Thereafter the failure mode of these tubes was similar to that of tubes [$90/0_4/90$] with formation of folds (Fig. 8). Nevertheless, the folding propagation was stable with regard to the force-displacement curve of each of the tubes (Fig. 5 (d)). However, there were about half as many folds on the configuration [$90/0_4/90$] (discussed in section 3.1.5), which explains the smaller number of oscillations on the force displacement curve. As with composite laminates, the number of 0° plies was important. Therefore, the energy absorbed and the SEA of these tubes (1 619 J and 31.6 J/g) decreased with respect to the configuration [$90/0_4/90$] (726 J and 18 J /g). The CFE also decreased slightly from 0.71 to 0.62.

Fig. 8: First line: failure initiation of tubes [$90_2/0_2/90_2$] after 23.8 mm of crushing; second line: failure patterns after 60 mm of crushing and, last line: post-mortem views.

3.1.4. Results for [$0_4/90_2$] tubes.

The objective for this last configuration was to observe the influence of the position of the layers at 90°. Fold formation was again present for the mode of ruin of these tubes. At the beginning of the crushing, it was found that the tubes lost their cylindrical geometry, which became oval, corresponding to the formation of a fold in diamond mode, probably because of the unsymmetrical stacking, which created local membrane/bending coupling. At a given height of the tube and on the same plane, two inside folds were created facing each other while, perpendicularly, there were also two folds facing each other, but outwards (Fig. 9). So, on this same plane, 4 folds were visible.

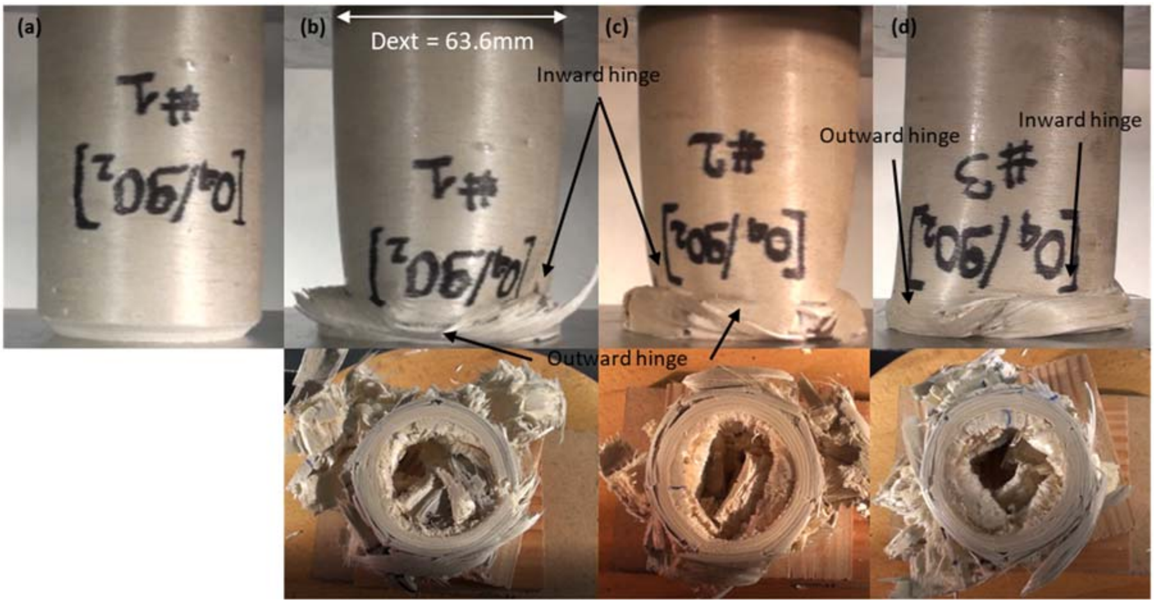

Fig. 9: Initiation of failure mode of $[0_4/90_2]$ tubes. (a) #1 pristine, (b) #1, (c) #2 (d) #3 between 26 and 27mm of crushing.

The diamond shape appeared at the start of crushing and corresponded to the formation of the plateau on the force-displacement curve (around 30 mm of crushing) (Fig. 5 (c)). Furthermore, the number of folds for this configuration was almost twice that with the $[90/0_4/90]$ configuration and, again, can explain why the oscillations on the force-displacement curve were less marked. The influence of the position of the layer at 90° is not negligible and has its importance for the amount of energy absorbed. From the configuration $[90/0_4/90]$ to configuration $[0_4/90_2]$, an average loss of 87.6 J for EA and 10.3 J/g for SEA should be noted. The CFE dropped by 0.19. Having a 90° fold inside and outside clearly stabilized the fibres at 0° and induced better confinement than in the case where folds were located outside only.

3.1.5. Discussion on the crushing patterns (static).

Having no layers oriented at 90°, the tubes $[0_6]$ crushed in a very unstable way. The initiation was marked by the appearance of bundles characterizing cracking between the fibres in the longitudinal direction. The propagation of splitting in the direction of the tube led to a significant loss of stiffness of the tube, cutting the tubes into bundles (Fig. 6). As the tubes no longer satisfied the structural criterion, the initial crushing length of 90 mm was not respected; the test was interrupted on tubes # 1 and # 2 (zero compression force). With a layer oriented at 90°, crushing was stabilized, and a gain in absorbed energy was observed.

Nevertheless, it is difficult to analyse the situation by looking only at the outer pattern of the tubes from a macroscopic point of view. Therefore, some tubes were cut lengthwise into two half-tubes to gain access to more information about their failure modes (Fig. 10 (a)).

Some differences between the two configurations [90/0_4/90] and [90_2/0_2/90_2] were still present. The number of folds was higher for the [90/0_4/90] tubes (Fig. 10 (a)). Other authors [43] have found that inserting foam on thin-walled tubes reduces the buckling length of the folds, thereby increasing their number, and also increases the crushing force. In our case, we can assume that the presence of more fibres at 0° required a greater crushing force, which generated an increase in the number of folds and therefore more energy absorbed.

For [90/0_4/90] tubes, transversal cracking (i.e. in the thickness of the tube) was visible in the wall of the tube # 1 (Fig.10 (b)). This crack may explain the drop in the crushing force in the plate after the peak load. Such cracks were also found in the other two configurations [0_4/90_2] and [90_2/0_2/90_2]. For tubes [90/0_4/90] # 2 and # 3 and [90_2/0_2/90_2] - # 3, the fibre breakages observed in layers oriented at 90° allowed the appearance of a vertical crack creating petals, although the global failure mode was by local buckling (Fig. 10 (a)). In Fig. 10, some 0° layers can be seen to be broken, probably because of the high bending stresses due to the local hinges. However, most of the time, the wooden layers support large local deformations. Delaminations are also observed everywhere, mostly at the 0°/90° interface but it is hard to explain their onset in the failure scenario (before or after the peak load) in this post-mortem analysis.

Finally, an elastic return was observed in the length of the tubes. Since the tubes were not 100% damaged, some structural integrity of the tubes remained. Therefore, the tubes unfolded after the release of the compression force. The elastic return is not negligible: the remaining length of the crushed tubes should have been 30 mm, whereas a residual length of around 60 mm was measured.

Finally, the overall failure patterns of each configuration having two of the layers oriented at 90° are very similar to each other (local buckling formation, delamination 0/90, etc.) but there are many discrepancies, which can be attributed to several parameters:

- The fact that the tubes were manufactured manually may have introduced sources of variability: the process could have led to a deviation of the angles of the fibres (0° or 90°), due to either the cutting or the winding of the veneers, and the bonding could exhibit some defects.
- In addition to being anisotropic, wood is a very heterogeneous material. It therefore shows considerable variability in its properties: humidity, density, spring / winter wood, etc.

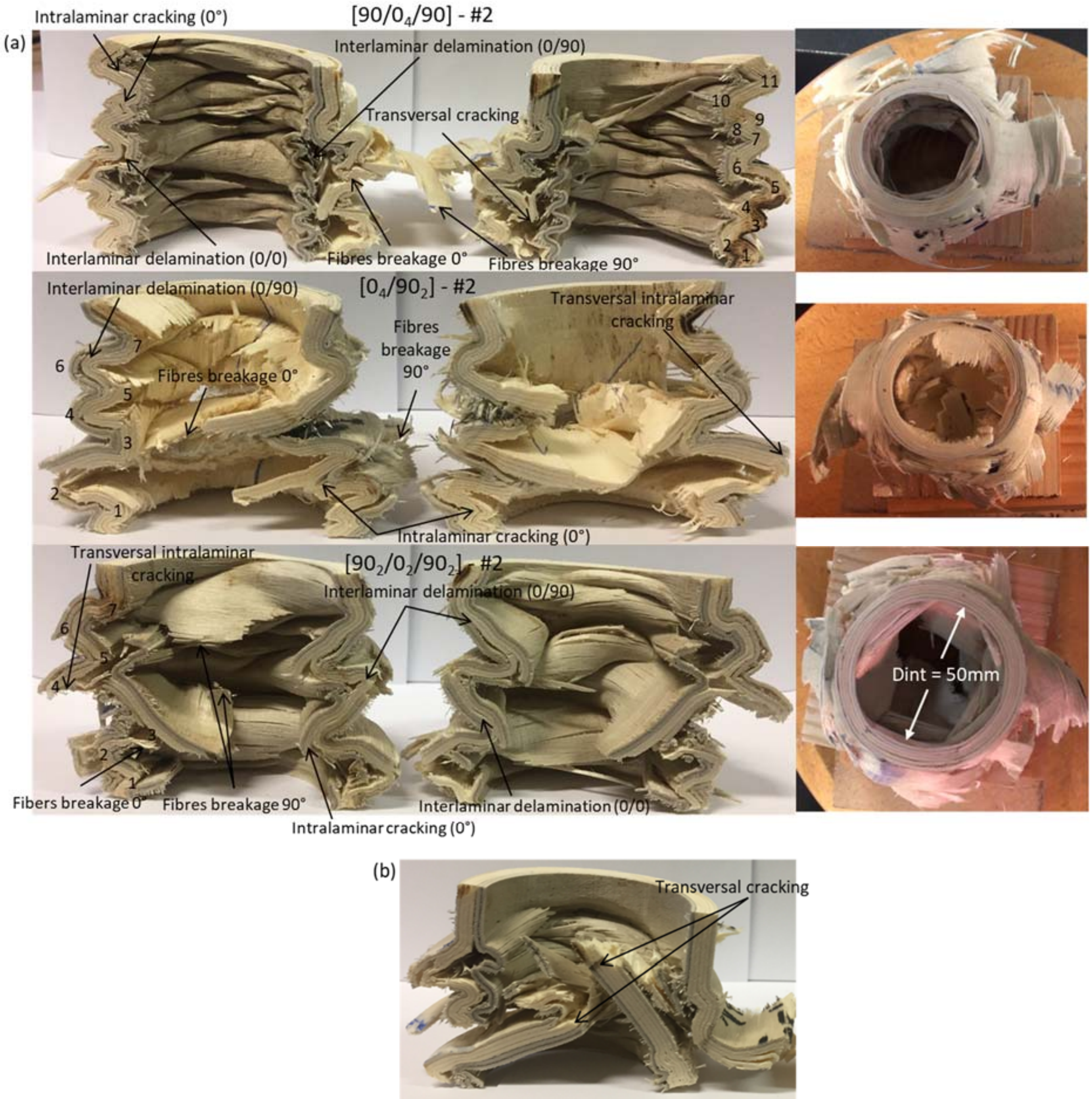

Fig. 10: (a) Static crushing modes – the left and right pictures are from the same sample. The figures on the pictures are used to count the number of folds. (b) Delamination, photo of half-tube [90/0$_4$/90] #1

3.2. Dynamic crushing

The configuration of the tubes having the best characteristics in terms of energy absorption (EA, SEA and CFE) in static tests was kept for the dynamic tests. Six tubes [90/0_4/90] were crushed in order to see the difference in behaviour and energy absorption in static and dynamic situations. Results are given in Tab. 1 and the six dynamic crushing force-displacement curves of the tubes [90/0_4/90] are shown in Fig.11. The general shape of the force-displacement curves is identical to the static case, with the same three phases of initiation, transition and plateau. In terms of performance, two groups of tubes can be identified: tubes 1, 2 and 6 have a SEA between 23.1 and 24.9 J / g while tubes 3, 4 and 5 have a SEA of 31 to 34.9 J / g. From the manufacturing point of view, no significant defects that could explain this performance gap were observed from one tube to another. Therefore, this difference can be attributed, as in static crushing, to the variability of the material.

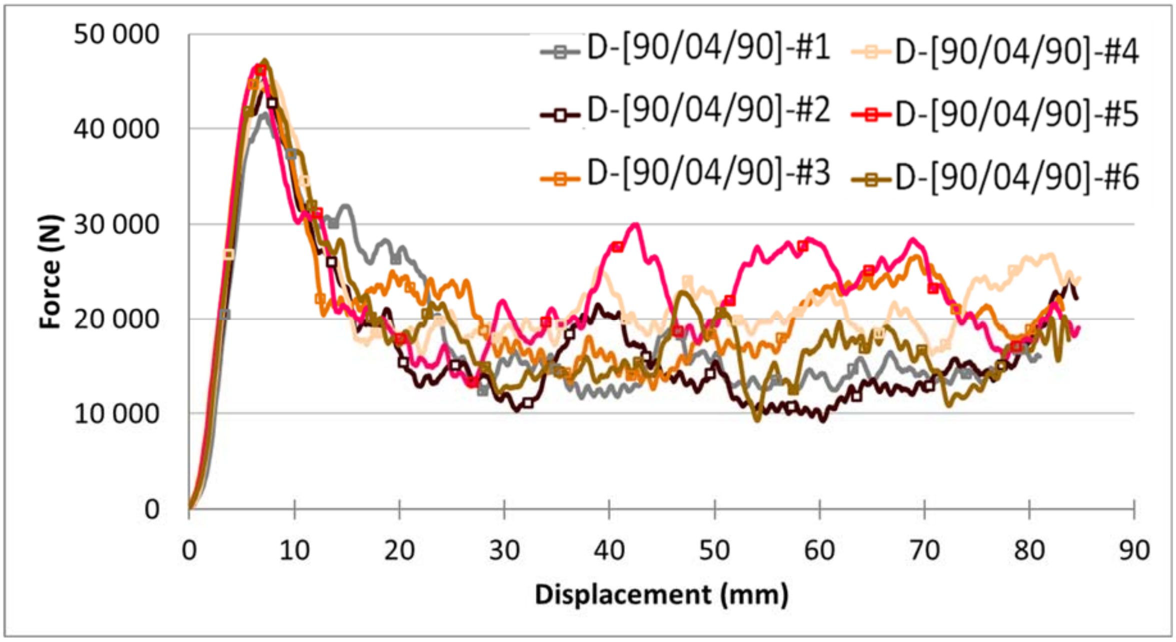

Fig. 11: Dynamic force-displacement curves for tubes [90/0_4/90]

The dynamic failure pattern is almost the same on the six specimens (Fig. 12).

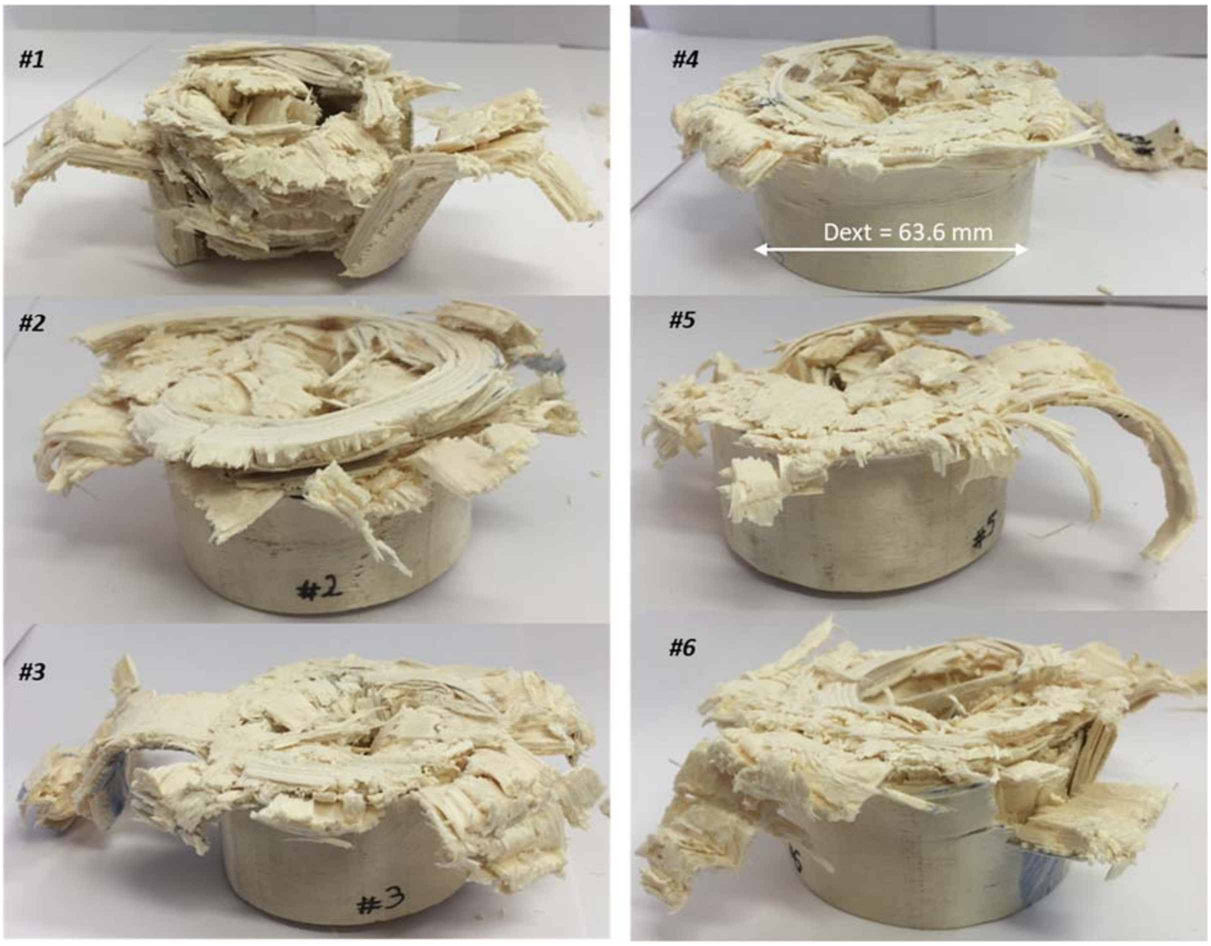

Fig. 12: Dynamic crushing modes of all 6 tubes [90/0_4/90]

Crushing is initiated by the formation of a local fold on the side of the chamfer, recalling the mode of ruin of the tubes in static tests. The formation of the folds generates delaminations, intralaminar cracking and probably wood fibre failures, which divide the tubes into bundles (Fig. 13).

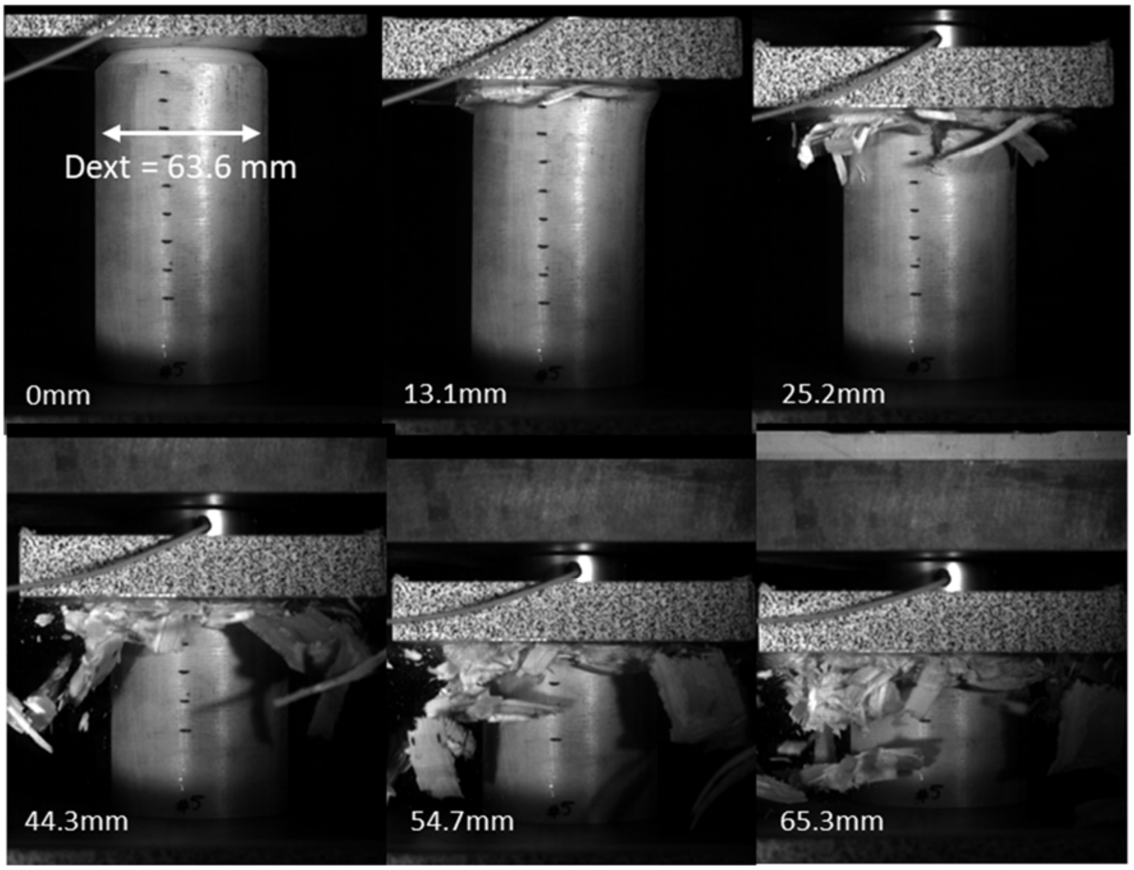

Fig. 13: Failure scenario of tube #5

The failures then propagate due to local bending until local fragmentation forms macroscopic debris (Fig. 13). Small debris (almost dust) was also observed. The separation of the tube into a bundle and the bending of the latter is analogous to splaying. The observation of macroscopic debris allowed us to note that splaying did not occur in an identical way for all the tubes. By cutting the tubes it was possible to provide a more precise explanation of the ruin of the tubes used in dynamic tests (Fig. 14). The presence of debris during the crushing is responsible for the splaying as the debris forces the upper intact part to separate and splay. When crushing different configurations of carbon-epoxy fibre plates, Guillon [23] also found an accumulation of debris causing a damaged flare. Depending on the position, the debris will condition the number of folds that splay inward or outward (Fig. 15).

The formation of bundles and their bending allow the creation of petals. The formation of petals has been observed on crushed CFRP tubes for a long time [27] (Fig. 15). Splaying is also initiated by an interlaminar crack that dissociates the tubes into bundles. Again, these bundles bend and then form the petals. The geometric shape of the petals (length, width, thickness) are influenced by many parameters such as stiffness, ultimate stresses, tube diameter, and wall thickness.

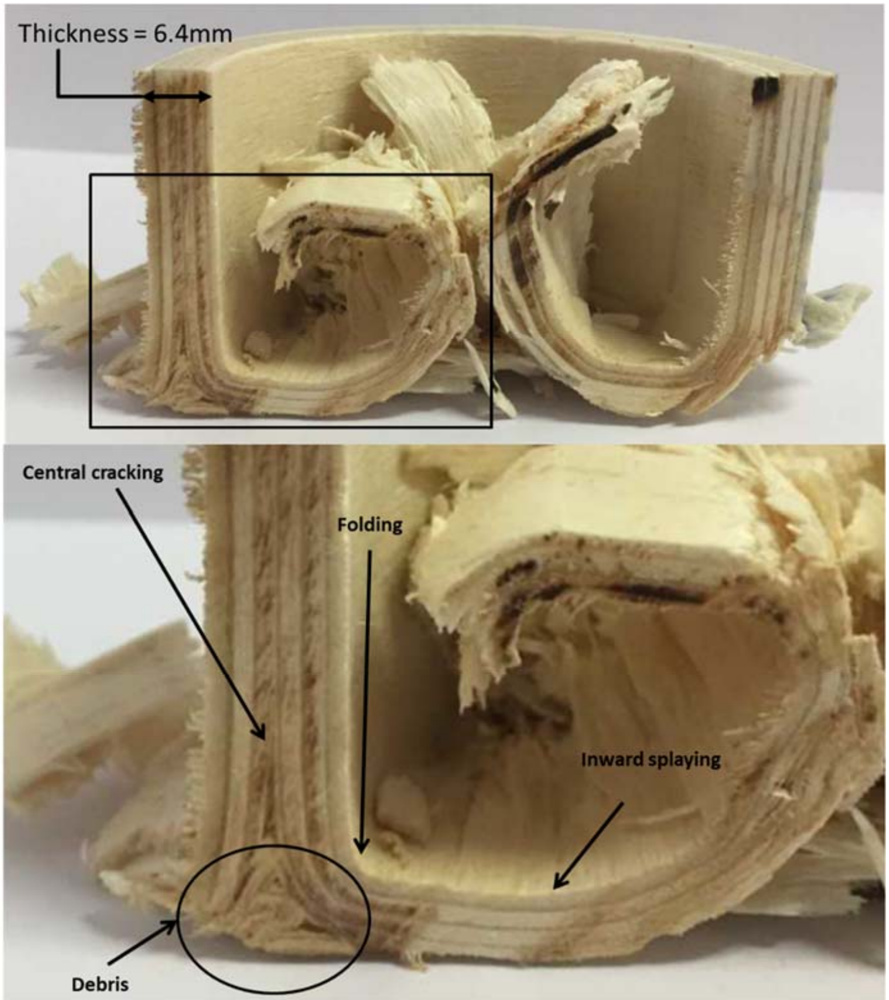

Fig. 14: Tube #5 cross section

Fig. 15: Petal failure mode for poplar wood.

3.3. Comparison of static and dynamic crushing

All the test curves for the [90/0₄/90] specimens are merged in Fig. 16.

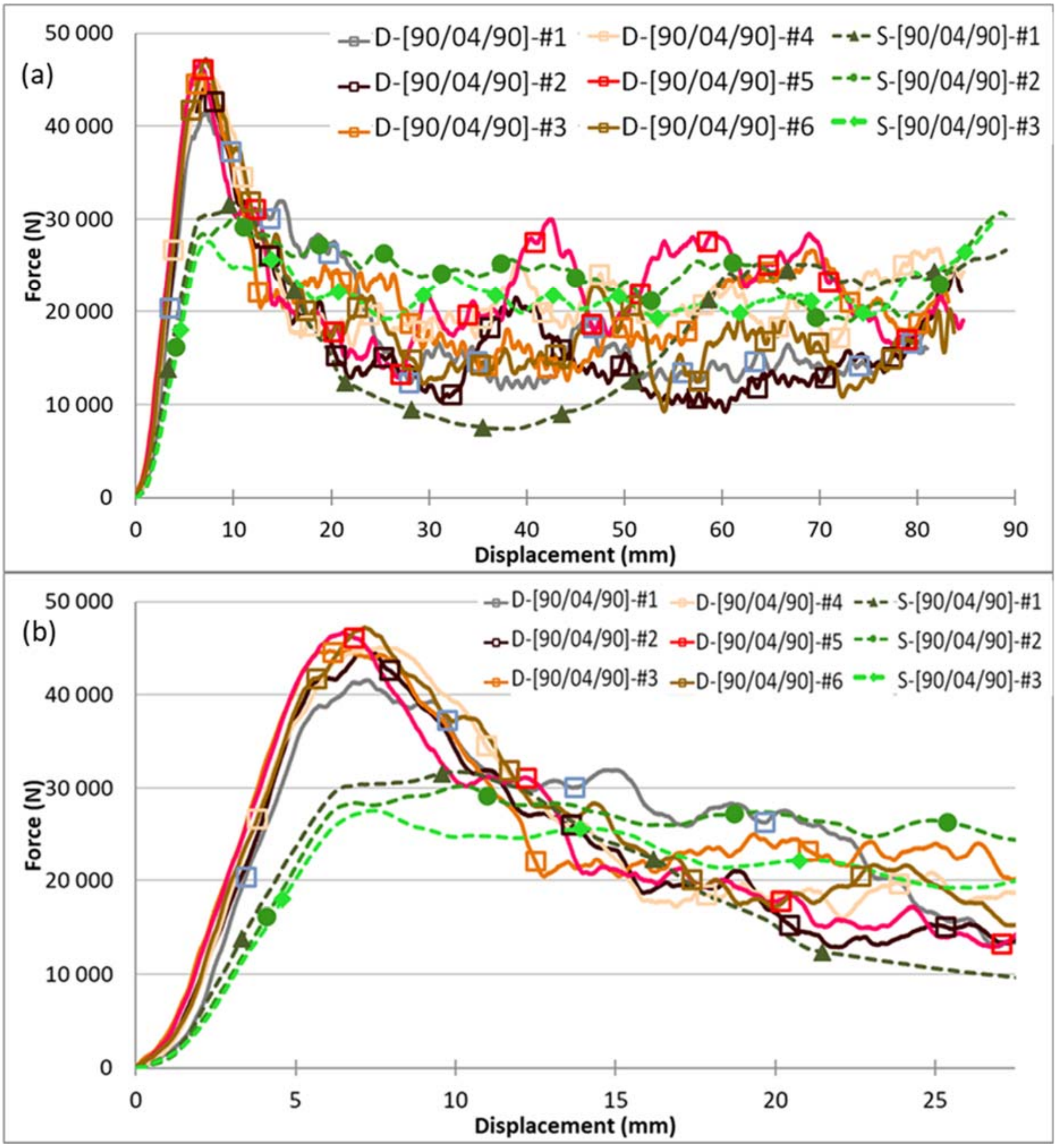

Fig. 16: (a) Comparison of static and dynamic crush curves (S-for static and D- for dynamic) (b) Zoom on the transition region

The first major difference between the static and dynamic curves is the value of the peak load: it is much higher in dynamic (45,084 N) than in static tests (29,837 N). The second difference is the apparent stiffness of the tube during pseudo-linear loading. The dynamic stiffness (pseudo-linear slope) is 88% higher than the static stiffness (515 MPa and 970 MPa for static and dynamic, average values). These two differences have also been found in drop weight tests on poplar [13] and in Hopkinson tests on beech and spruce [10,11]. The transition phase between the peak load and the plateau is also more marked in dynamic than in static crushing. In static situations, as soon as the peak load passes, the plateau is present. Although the plateau can be decreasing, it is obtained between 5 and 10 mm in static (Fig. 16 (b)). The peak load is obtained at substantially the same displacement as in static tests, except that the dynamic transition phase ends at around 15 mm (12.5 mm for the shortest transition phase, obtained for tube 4). The end of the pseudo-linear phase, corresponding to the moment when the first damage occurs and when there is a fall in force, is around 6-7 mm of displacement for static or dynamic tests. This value corresponds closely to the value of the height of the chamfer, which therefore appears to be responsible for the end of this phase.

In addition, the difference between the maximum force and the minimum force observed on the plate is greater in dynamic loading (up to 15,600 N) than in static (11,700 N if the unstable crushing of tube # 1 is omitted). On the other hand, due to the increase in the peak load, the CFE ratio decreases in dynamic loading, from 0.71 to 0.40. Finally, the other performance levels (Tab. 1), whether for the average force (21,019 N in static - 17,939 N in dynamic), the energy absorbed (1,632 J in static - 1,618 J dynamic) or the SEA (31.6 J/g static - 28.5 J/g dynamic), are almost identical between static and dynamic crushing. During Hopkinson or weight-down crushing to assess the effect of the speed of the stress on the behaviour of the wood material [9–13], it was found that the average stress increased with the dynamic effect, causing an increase of the energy absorbed and therefore of the SEA.

In this study, the dynamic failure mode differs from the static one. In static, the crushing is stable with creation of folds while the dynamic tubes have a failure initiation identical to the static (formation of a fold) but subsequent propagation is by splaying and fragmentation creating macroscopic and microscopic debris (Fig. 17).

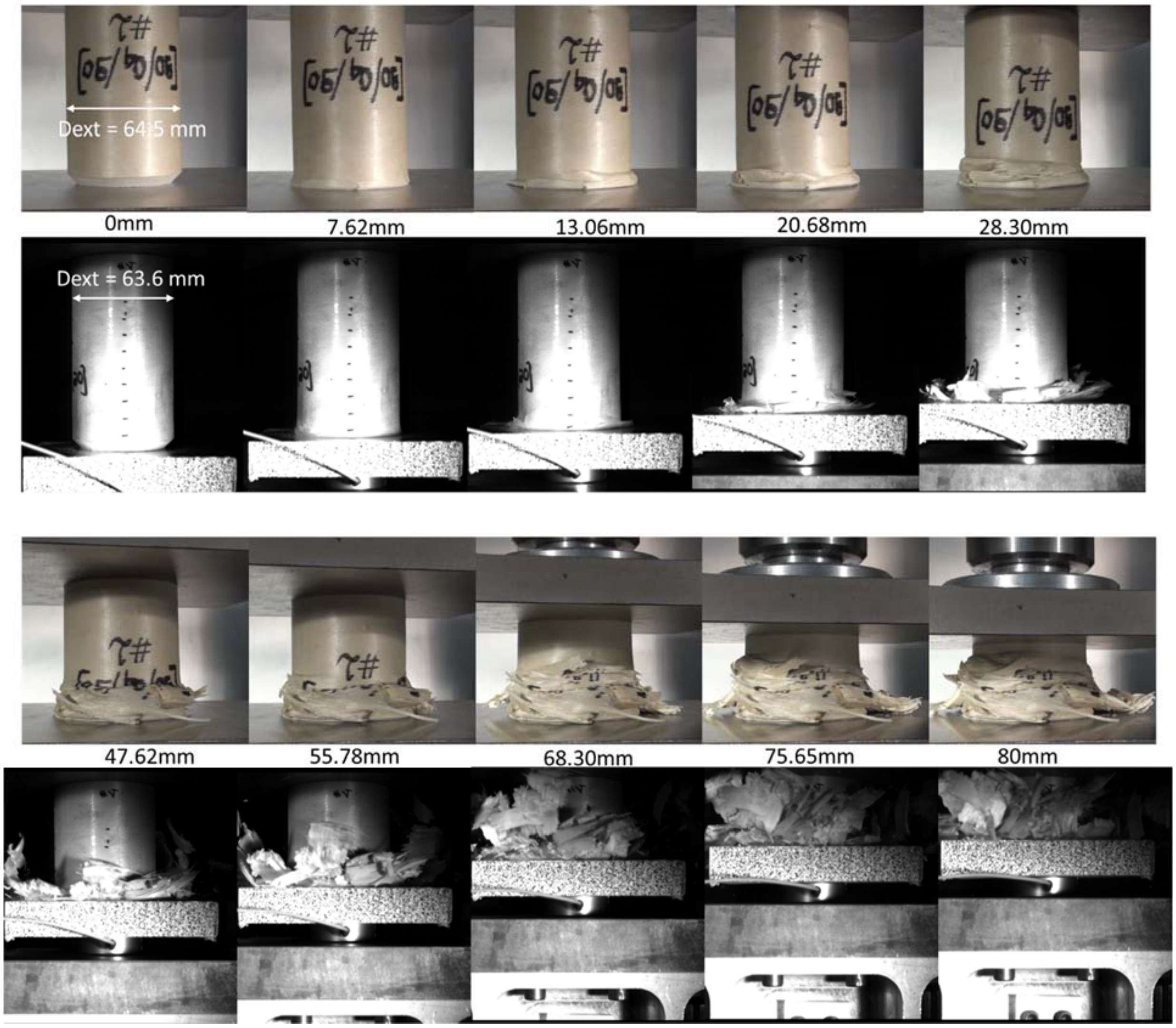

Fig. 17: Comparison of the failure scenario between a static and a dynamic tests at iso-displacement [90/0$_4$/90] - #2 specimen for static – [90/0$_4$/90] - #1 specimen for dynamic.

The change in static-dynamic failure mode can be explained by the viscoelastic nature of wood. Its constituents (lignin, cellulose, and hemicellulose) have a behaviour that changes with the strain rate. This can be shown by the increase in the apparent stiffness (mentioned above). Therefore, in static crushing, the wood has a ductile character, which enables folds to form, while in dynamic, the fragile character takes over and generates a fragile mode with the creation of multiple macroscopic debris. In addition, the glue can have an important influence. It is thus difficult to conclude that ($F_{plateau}$, EA_{tot_80mm}, $SEA_{plateau}$) are almost identical between the static and the dynamic regimes.

The transition from static to dynamic crushing is also an issue for composite materials, particularly as far as the evolution of performances is concerned. Do they increase or decrease in dynamic crushing? The works of Farley and Jones [31] attribute the increase in crash characteristics to the dependence of material properties on the strain rate, especially for Kevlar fibres but also for the matrix. In their study, Mamalis et al. [44] obtained different failure modes between static and dynamic loading, thus explaining the variation in performance. McGregor et al. [45] attribute the lower performance in dynamic loading to the fact that there is more transverse shear in the corners of the tubes in dynamic failure, associated with a deterioration of the fibre/matrix interface and a fragile behaviour of the matrix. David et al. [46] observed that the length of the petals was longer in static loading, leading to more cracking, and increased friction in delamination and at the interface of the plates. In dynamic loading, the matrix becomes more fragile, its stiffness increases and its toughness decreases, leading to a reduction in the splaying lengths. Finally, Brighton et al. [47] attribute the decrease in dynamic properties to the radius of curvature of the petals, which is smaller in static and leads to more damage.

3.4 Summary

According to the literature, in terms of SEA, wood shows poorer performance than composite or metallic materials but remains interesting thanks to its carbon footprint, its recyclability, and its material cost, which is very low compared to those of composite materials (the cost of poplar veneer I214 in 1240x2200 mm^2 format is about € 2.5/veneer while that of CFRP is € 34/m^2 on average). The SEA of tubes made of carbon fibre composite materials with an epoxy resin ranges from 38 J/g [48], with an internal diameter of 50 mm and a ±45° and 0° stacking sequence, to 140 J/g, with the same internal diameter but a $[(0/90)/(0)_8/(0/90)]$ sequence [49] (Fig. 18) and can reach 227 J/g in presence of PEEK resin with a tube 55 mm in diameter and 2.66 mm thick [50]. Glass fibres have a slightly lower potential, from 21 J/g [51] and 87 J/g [52] for semi-hexagonal profiles with unidirectional plies oriented at 0° and 90° to a 39.3 mm diameter tube of 3 mm thickness, to a maximum of 195 J/g for a PEEK resin [53] obtained on a 55 mm diameter tube with a thickness of 2.65 mm and fibre orientation of ±10°. If we consider metallic materials, the SEA can vary from 34 to 88 J/g [54,55], the maximum SEA being obtained with Al 6061 on a 38.1 mm diameter tube with 2.4 mm thickness. Flax tubes ranging from 36 mm to 82 mm in diameter have shown an interesting potential varying from 7 to 42 J/g [30]. Researchers have also tried to recycle wood chips by integrating them as core material in PVC (external diameter of 84 mm with 2.3 mm wall thickness) and aluminium (38 mm inner diameter and 1.2 mm wall thickness) tubes, and have obtained SEA values between 9 and 17 J/g [56, 57]. Finally, with 100 x 100 x 15.5 mm^3 plates, as a core material associated with glass fibre skins, solid balsa has shown a SEA of between 12 and 20 J/g depending on the triggers used [58].

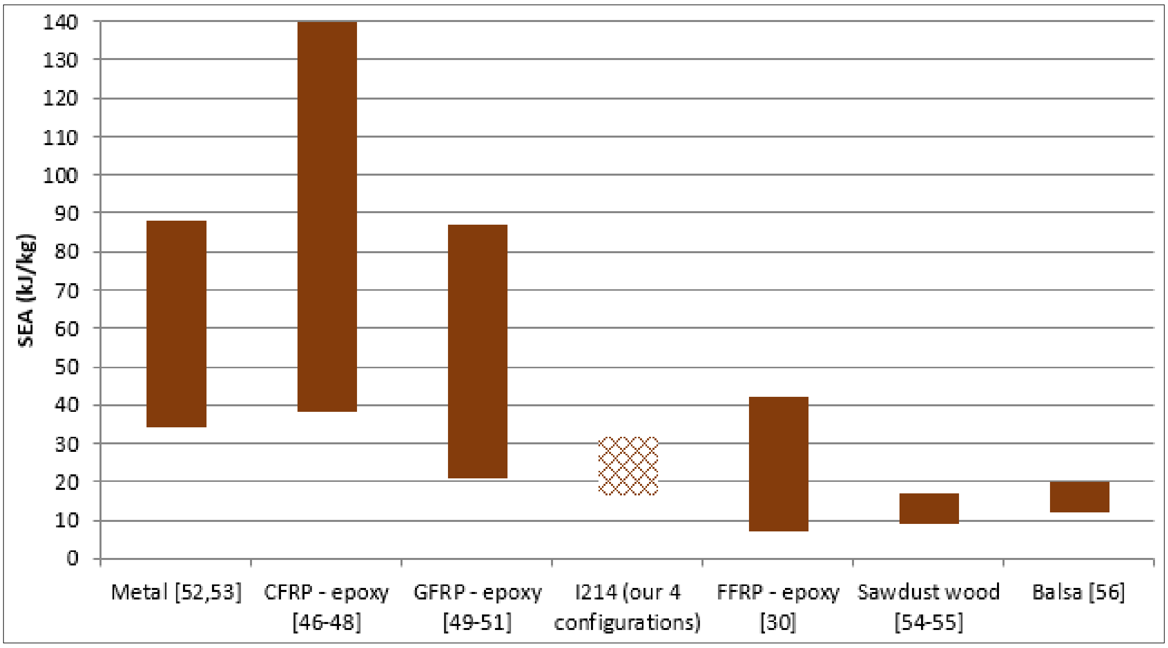

Fig. 18: SEA of various materials

4. Conclusions and perspectives

Static and dynamic crushing performances are quite promising for a natural and environmentally friendly material like wood. The tests have shown that:

- Orienting all the poplar layers at 0° is not a good choice as it generates an unstable failure mode with very low energy absorption.
- As soon as a 90° layer is present outside and inside (or only outside), this produces a "hoop" effect and the tube will have a stable crushing mode with a plateau whatever the configuration.

- Too many layers at 90° are not necessarily effective in terms of the amount of energy absorbed: loss of 43% of SEA between the configurations [$90_2/0_2/90_2$] and [$90/0_4/90$].
- The position of the layers at 90° also has an influence on the amount of energy absorbed. In fact, in the configurations [$0_4/90_2$] and [$90/0_4/90$], a gain of 33% of SEA is obtained by completely confining the layers at 0°. The "hoop" effect found for composite materials is also found here.
- In terms of static failure modes, the presence of 90° plies allows successive and asymmetrical formation of folds generated by local buckling. In dynamic tests, the failure mode changes, with the apparition of splaying and fragmentation generating macroscopic and microscopic debris.
- The best of the static configurations studied, and used in dynamic tests, was [$90/0_4/90$], which reached an average absorbed energy of 1 632 J in static and 1 618 J in dynamic configurations, with an average SEA of 30 J/g.
- In dynamic testing, the peak load and the stiffness are significantly increased and the SEA is almost identical. The CFE is also significantly lower in dynamic. Finally, the transition phase is more significant in dynamic than in static loading.

These results are very promising for the future of the use of wood-based eco-materials for crash applications. Although the levels of SEA reached are a quarter of those obtained on the best composite materials, the composite materials are 40 times as expensive as the wood-based ones. In addition, the poplar selected for this study is one of the least mechanically efficient woods and it is likely that better quality woods would have higher SEA. In addition, to better understand the crush behaviour of wood tubes, advanced modelling is necessary. A very limited number of papers have dealt with the subject [17] so far and a research effort has to be made to develop material damage models for wood plies, together with efficient modelling strategies.

5. Acknowledgements

The authors thank the French Government for providing financial support and the Garnica company for providing I214 veneers for this study.

6. References

[1] Laboratory FP. Wood Handbook Wood as an Engineering Material. United States Department of Agriculture Forest Service; 2010.

[2] Bergman R, Puettmann M, Taylor A, Skog KE. The Carbon Impacts of Wood Products. Forest Products Journal: 2014;64:220-231. https://doi.org/10.13073/FPJ-D-14-00047

[3] Bucci V, Corigliano P, Crupi V, Epasto G, Guglielmino E, Marinò A. Experimental investigation on Iroko wood used in shipbuilding. Proceedings of the Institution of Mechanical Engineers, Part C: Journal of Mechanical Engineering Science 2017;231:128–39. https://doi.org/10.1177/0954406216674495.

[4] Zenkerts D. The handbook of sandwich construction. Engineering Materials Advisory Services Ltd. United Kingdom: 1997.

[5] Susainathan J, Eyma F, De Luycker E, Cantarel A, Castanie B. Manufacturing and quasi-static bending behavior of wood-based sandwich structures. Composite Structures 2017;182:487–504. https://doi.org/10.1016/j.compstruct.2017.09.034

[6] Butler N. Computer modelling of wood-filled impact limiters. Nuclear Engineering and Design 1994;150:417 424; https://doi.org/10.1016/0029-5493(94)90161-9

[7] CANPLY. Eléments de calcul du contreplaqué 1997.

[8] Johnson W. Historical and Present-Day References Concerning Impact on Wood. International Journal on impact Engineering 1986; 4:161-174. https://doi.org/10.1016/0734-743X(86)90003-5.

[9] Reid S.R., Peng C. Dynamic uniaxial crushing of wood. International Journal on impact Engineering 1997; 19:531-570. https://doi.org/10.1016/S0734-743X(97)00016-X

[10] Wouts J, Haugou G, Oudjene M, Morvan H, Coutellier D. Strain rate effects on the compressive response of wood and energy absorption capabillities - Part B: Experimental investigation under rigid lateral confinement. Composite Structures 2018. https://doi.org/10.1016/j.compstruct.2018.07.001.

[11] Wouts J, Haugou G, Oudjene M, Coutellier D, Morvan H. Strain rate effects on the compressive response of wood and energy absorption capabilities – Part A: Experimental investigations. Composite Structures 2016;149:315–328. https://doi.org/10.1016/j.compstruct.2016.03.058.

[12] Pang S, Liang Y, Tao W, Liu Y, Huan S, Qin H. Effect of the Strain Rate and Fiber Direction on the Dynamic Mechanical Properties of Beech Wood. Forests 2019, 10(10), 881; https://doi.org/10.3390/f10100881

[13] Adalian C, Morlier P. “WOOD MODEL” for the dynamic behaviour of wood in multiaxial compression. Holz Als Roh- Und Werkstoff 2002;60:433–9. https://doi.org/10.1007/s00107-002-0333-x.

[14] Demircioğlu TK, Balıkoğlu F, Inal O, Arslan N, Ataş A. Experimental investigation on low-velocity impact response of woodskinned sandwich composites with different core configurations. Materials Today Communications 2018;17:31-39. https://doi.org/10.1016/j.mtcomm.2018.08.003

[15] Smardzewski J. Wooden sandwich panels with prismatic core – Energy absorbing capabilities; Composite Structures 2019;230:111535. https://doi.org/10.1016/j.compstruct.2019.111535

[16] Susainathan, J., Eyma, F., De Luycker, E., Cantarel, A., Castanie, B. Experimental investigation of impact behavior of wood-based sandwich structures. Composites Part A: Applied Science and Manufacturing 2018;109,10-19. https://doi.org/10.1016/j.compositesa.2018.02.029

[17] Susainathan, J., Eyma, F., De Luycker, E., Cantarel, A., Castanie, B. Numerical modeling of impact on wood-based sandwich structures. Mechanics of Advanced Materials and Structures, on line, https://doi.org/10.1080/15376494.2018.1519619

[18] Susainathan J, Eyma F, De Luycker E, Cantarel A, Bouvet C, Castanie B. Experimental investigation of compression and compression after impact of wood-based sandwich structures. Composite Structures 2019;220:236–49. https://doi.org/10.1016/j.compstruct.2019.03.095.

[19] Nguyen XT, Hou S, Liu T, Han X. A potential natural energy absorption material – Coconut mesocarp: Part A: Experimental investigations on mechanical properties. International journal of mechanical sciences, 2016, 115-116: 564-573. https://doi.org/10.1016/j.ijmecsci.2016.07.017

[20] Liu T, Hou S, Nguyen X, Han X. Energy absorption characteristics of sandwich structures with composite sheets and bio coconut core. Composites Part B: Engineering, 2017, 114: 328-338. https://doi.org/10.1016/j.compositesb.2017.01.035

[21] Lu C, Hou S, Zhang Z, Chen J, Li Q, Han X. The mystery of coconut overturns the crashworthiness design of composite materials International journal of mechanical sciences, 2020, 168: 105244. https://doi.org/10.1016/j.ijmecsci.2019.105244

[22] Neveu F, Castanié B, Olivier P. The GAP methodology: A new way to design composite structures Materials & Design 2019;172:107755. https://doi.org/10.1016/j.matdes.2019.107755

[23] Guillon D. Etude des mécanismes d'absorption d'énergie lors de l'écrasement progressif de structures composites à base de fibre de carbone. PhD Thesis. Institut Supérieur de l'Aéronautique et de l'Espace, ISAE, Ecole doctorale : Mécanique, énergétique, génie civil et procédés, 2008.

[24] Kim J-S, Yoon H-J, Shin K-B. A study on crushing behaviors of composite circular tubes with different reinforcing fibers. International Journal of Impact Engineering 2011;38:198-207. https://doi.org/10.1016/j.ijimpeng.2010.11.007

[25] Ataabadi PB, Karagiozova D, Alves M. Crushing and energy absorption mechanisms of carbon fiber-epoxy tubes under axial impact. International Journal of Impact Engineering 2019;131:74-189. https://doi.org/10.1016/j.ijimpeng.2019.03.006

[26] Wang Y, Feng J, Wu J, Hu D. Effects of fiber orientation and wall thickness on energy absorption characteristics of carbon-reinforced composite tubes under different loading conditions. Composite Structures 2016;153:356–368. https://doi.org/10.1016/j.compstruct.2016.06.033.

[27] Hamada H, Coppola JC, Hull D, Maekawa Z, Sato H. Comparison of energy absorption of carbon/epoxy and carbon/PEEK composite tubes. Composites 1992;23:245–252. https://doi.org/10.1016/0010-4361(92)90184-v.

[28] Song H-W, Du X-W, Zhao G-F. Energy Absorption Behavior of Double-Chamfer Triggered Glass/Epoxy Circular Tubes. J Compos Mater 2002;36:2183–98. https://doi.org/10.1177/0021998302036018515.

[29] Hu D, Zhang C, Ma X, Song B. Effect of fiber orientation on energy absorption characteristics of glass cloth/epoxy composite tubes under axial quasi-static and impact crushing condition. Composites Part A: Applied Science and Manufacturing 2016;90:489–501. https://doi.org/10.1016/j.compositesa.2016.08.017.

[30] Yan L, Chouw N. Crashworthiness characteristics of flax fibre reinforced epoxy tubes for energy absorption application. Materials & Design 2013;51:629–640. https://doi.org/10.1016/j.matdes.2013.04.014.

[31] Farley GL, Jones MR. Energy absorption capability of composite tubes and beams. PhD Thesis. NASA TM 10634, 1989.

[32] Hull D. A unified approach to progressive crushing of fibre-reinforced composite tubes. Composites Science and Technology 1991;40:377–421. https://doi.org/10.1016/0266-3538(91)90031-j.

[33] Kindervater CM. Energy absorption of composites as an aspect of aircraft structural crash-resistance. Developments in the Science and Technology of Composite Materials, Springer Netherlands; 1990, p. 643–651. https://doi.org/10.1007/978-94-009-0787-4_89.

[34] Thornton PH, Edwards PJ. Energy absorption in composite tubes. Journal of Composite Materials 1982;16:521–545. https://doi.org/10.1177/002199838201600606.

[35] Garnica. http://www.garnica.one/en. Accessed 02 April 2020

[36] Baldassino N, Zanon P, Zanuttini R. Determining mechanical properties and main characteristic values of Poplar plywood by medium-sized test pieces . Materials and Structures 1998;31(1): 64-67. https://doi.org/10.1007/BF02486416.

[37] Fang CH, Mariotti N, Cloutier A, Koubaa A, Blanchet P. Densification of Wood Veneers by Compression Combined with Heat and Steam. European Journal of Wood and Wood Products 2012; 70 (1-3):155-63. https://doi.org/10.1007/s00107-011-0524-4.

[38] Siromani D, Henderson G, Mikita D, Mirarchi K, Park R, Smolko J, et al. An experimental study on the effect of failure trigger mechanisms on the energy absorption capability of CFRP tubes under axial compression. Composites Part A: Applied Science and Manufacturing 2014;64:25–35. https://doi.org/10.1016/j.compositesa.2014.04.019.

[39] Blazy J-S. Comportement mécanique des mousses d'aluminium : caractérisations experimentales sous sollicitations complexes et simulations numériques dans le cadre de l'élasto-plasticité compressible. PhD Thesis. Ecole Nationale Supérieure des Mines de Paris, 2003.

[40] Andrews KRF, England GL, Ghani E. Classification of the axial collapse of cylindrical tubes under quasi-static loading. International Journal of Mechanical Sciences 1983;25:687–696. https://doi.org/10.1016/0020-7403(83)90076-0.

[41] Al Galib D, Limam A. Experimental and numerical investigation of static and dynamic axial crushing of circular aluminum tubes. Thin-Walled Structures 2004;42:1103–37. https://doi.org/10.1016/j.tws.2004.03.001.

[42] Dubey DD, Vizzini AJ. Testing Methods for Energy Absorption of Kevlar/Epoxy. J Am Helicopter Soc 1999;44:179–87. https://doi.org/10.4050/JAHS.44.179.

[43] Baroutaji A, Sajjia M, Olabi A-G. On the recent crashworthiness performance of thin walled energy absorbers: recent advances and future developments. Thin-Walled Strucutres 118 137-163 2017.

[44] Mamalis AG, Manolakos DE, Ioannidis MB, Papapostolou DP. On the response of thin-walled CFRP composite tubular components subjected to static and dynamic axial compressive loading: experimental. Composite Structures 2005;69:407–420. https://doi.org/10.1016/j.compstruct.2004.07.021.

[45] McGregor C, Vaziri R, Poursartip A, Xiao X. Axial crushing of triaxially braided composite tubes at quasi-static and dynamic rates. Composite Structures 2016;157:197–206. https://doi.org/10.1016/j.compstruct.2016.08.035.

[46] David M, Johnson AF, Voggenreiter H. Analysis of Crushing Response of Composite Crashworthy Structures. Appl Compos Mater 2013;20:773–87. https://doi.org/10.1007/s10443-012-9301-8.

[47] Brighton A, Forrest M, Starbuck M, Erdman D, Fox B. Strain Rate Effects on the Energy Absorption of Rapidly Manufactured Composite Tubes. Journal of Composite Materials 2009;43:2183–200. https://doi.org/10.1177/0021998309344646.

[48] Schultz MR. Energy absorption capacity of graphite-epoxy composite tubes. Master's Thesis. Virginia Polytechnic Institute and State University, 1998.

[49] Chambe J, Bouvet C, Dorival O, Ferrero J. Energy absorption capacity of composite thin-wall circular tubes under axial crushing with different trigger initiations. Journal of Composite Materials 2019:002199831987722. https://doi.org/10.1177/0021998319877221.

[50] Hamada H, Ramakrishna S. Scaling effects in the energy absorption of carbon-fiber/PEEK composite tubes. Composites Science and Technology 1995;55:211–21. https://doi.org/10.1016/0266-3538(95)00081-X.

[51] Esnaola A, Ulacia I, Aretxabaleta L, Aurrekoetxea J, Gallego I. Quasi-static crush energy absorption capability of E-glass/polyester and hybrid E-glass–basalt/polyester composite structures. Materials & Design 2015;76:18–25. https://doi.org/10.1016/j.matdes.2015.03.044.

[52] Ochelski S, Gotowicki P. Experimental assessment of energy absorption capability of carbon-epoxy and glass-epoxy composites. Composite Structures 2009;87:215–24. https://doi.org/10.1016/j.compstruct.2008.01.010.

[53] Hamada H, Ramakrishna S. Effect of Fiber Material on the Energy Absorption Behavior of Thermoplastic Composite Tubes. Journal of Thermoplastic Composite Materials 1996;9:259–79. https://doi.org/10.1177/089270579600900304.

[54] Farley GL. Energy absorption of composite materials. Journal of Composite Materials 1983;17:267–279. https://doi.org/10.1177/002199838301700307.

[55] Saito H, Chirwa EC, Inai R, Hamada H. Energy absorption of braiding pultrusion process composite rods. Composite Structures 2002;55:407–417. https://doi.org/10.1016/s0263-8223(01)00160-x.

[56] Singace AA. Collapse behaviour of plastic tubes filled with wood sawdust. Thin-Walled Structures 2000;37:163–187. https://doi.org/10.1016/s0263-8231(00)00012-4.

[57] Kiran R, Khandelwal N, Tripathi P. Collapse behaviour and energy absorption of aluminium tubes filled with wood sawdust. International Journal of Engineering Research and Reviews 2014.

[58] Lindstrom A, Hallstrom S. Energy absorption of SMC/balsa sandwich panels with geometrical triggering features. Composite Structures 2010;92:2676–2684. https://doi.org/10.1016/j.compstruct.2010.03.018.